**DOI: 10.1063/5.0135407**

# Silicon anisotropy in a bi-dimensional optomechanical cavity

Cite as: APL Photon. 8, 056112 (2023); doi: 10.1063/5.0135407
Submitted: 18 November 2022 • Accepted: 2 May 2023 •
Published Online: 25 May 2023



Cauê M. Kersul,[1] Rodrigo Benevides,[1] Flávio Moraes,[1] Gabriel H. M. de Aguiar,[1] Andreas Wallucks,[2] Simon Gröblacher,[2] Gustavo S. Wiederhecker,[1] and Thiago P. Mayer Alegre[1,a)]

## AFFILIATIONS

[1] Gleb Wataghin Physics Institute, University of Campinas, 13083-859 Campinas, SP, Brazil
[2] Kavli Institute of Nanoscience, Department of Quantum Nanoscience, Delft University of Technology, Delft, The Netherlands

[a)] **Author to whom correspondence should be addressed:** alegre@unicamp.br

## ABSTRACT

In this work, we study the effects of mechanical anisotropy in a 2D optomechanical crystal geometry. We fabricate and measure devices with different orientations, showing the dependence of the mechanical spectrum and the optomechanical coupling on the relative angle of the device to the crystallography directions of silicon. Our results show that the device orientation strongly affects its mechanical band structure, which makes the devices more susceptible to orientation fabrication imperfections. Finally, we show that our device is compatible with cryogenic measurements, reaching a ground state occupancy of 0.25 phonons at mK temperature.





In the last decade, optomechanical crystal cavities have been shown to confine light and mechanical motion in sub-wavelength modal volumes, leading to high optomechanical coupling rates[1–3] ($g_0$) and long-lived mechanical excitations.[4,5] Through the careful choice of geometry and material, the photon–phonon interaction can be tailored, enabling applications not only in the classical realm, such as microwave phonon routing[6] and high-frequency phonon sources,[7] but also in the quantum domain, such as sideband ground-state cooling,[8] optomechanical quantum memories,[9] and remote quantum state transfer in mechanical dual-rail encoded qubits.[10] Most of the optomechanical crystal devices used in quantum experiments are based on suspended quasi-one-dimensional (1D) beam structures. These devices combine large optical and mechanical quality factors with high $g_0$ in a simple design. However, such quasi-1D geometries present a fundamental drawback since they usually do not have good thermal dissipation, and even the faintest light pulses can heat a device away from its mechanical ground state.[5,9] In contrast, quasi-two-dimensional (2D) structures[4,11,12] have already been demonstrated to have impressive optical quality factors[13] and could have much better thermal conductance. Nonetheless, few experimental works have focused on hypersonic (>GHz) quasi-2D optomechanical crystal[14,15] devices due to their more complex design and fabrication processes. In this case, material crystalline anisotropy, known to affect the performance of quasi 1D-optomechanical devices,[2,16,17] becomes even more important. In this work, we study, through simulation, fabrication, and measurements, the impacts of the mechanical anisotropy on a silicon-based cavity using the recently proposed design from Ref. 12. We then achieve the high optomechanical coupling and low-phonon number occupancy necessary for quantum experiments.

The device's geometry consists of a quasi-1D cavity composed of two lines of C-shaped holes facing each other and surrounded by a 2D triangular lattice of snowflake-shaped holes [Fig. 1(a)]. The snowflake structure allows for large optical and mechanical band gaps[18,19] that confine the modes within the C-shape region while still providing a good path for thermal dissipation compared to quasi-1D designs. The final devices, shown in Figs. 1(a) and 1(b), are based on a traditional top–bottom fabrication process using a 220 nm silicon-on-insulator (SOI) wafer. They are composed of: (i) a 10 $\mu$m-long suspended tapered waveguide that efficiently couples[20] light either from a lensed or tapered fiber to a 360 nm wide waveguide; (ii) a coupler region composed of eight transition cells, where the regular waveguide geometry is slowly morphed into the C-shape mirror unit cell, avoiding strong reflections due to impedance mismatching;

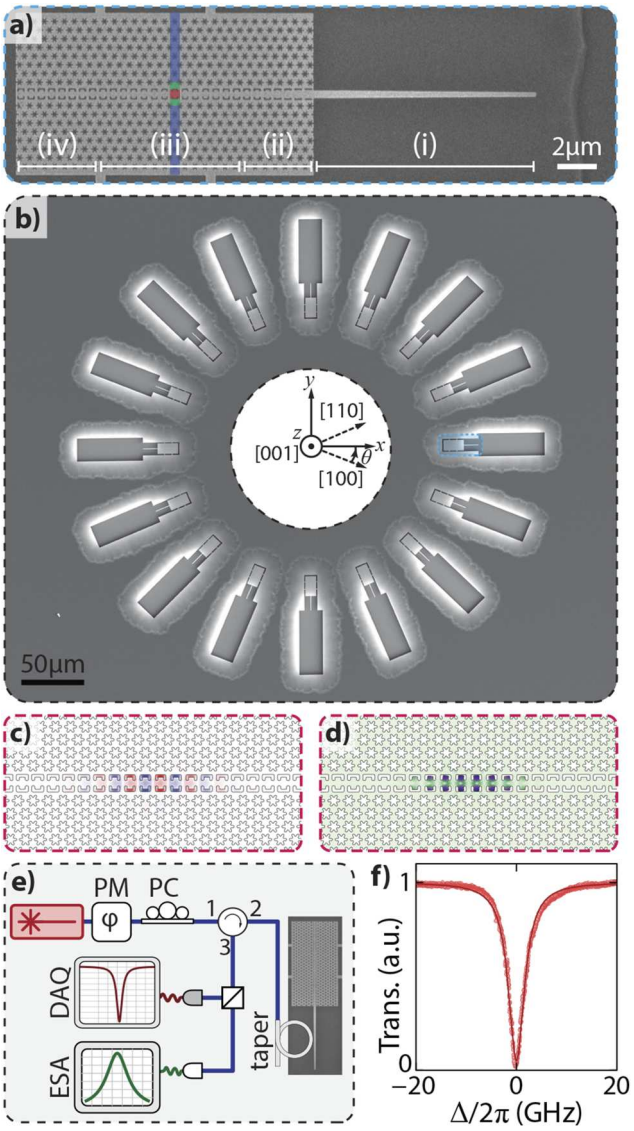


**FIG. 1.** (a) and (b) Scanning Electron Microscopy (SEM) images of a single and a set of angled devices. In (a), (i) indicates the tapered waveguide, (ii) the transition coupler, (iii) the defect, and (iv) the mirror region of our optomechanical crystal. The small mismatch between the snowflake and the C-shape unit cells improves mechanical confinement by shifting the snowflake bands to larger frequencies. (c) and (d) Electrical ($E_y$) and mechanical ($|\mathbf{u}|$) fields of the confined optical and mechanical modes, respectively. (e) Experimental setup used in the measurements. (f) Typical reflection signal of the optical resonance.

(iii) a symmetrical defect region composed of 14 cells, whose dimensions are varied from the mirror unit cell at its edges to the defect unit cell at its center, confining both optical [Fig. 1(c)] and mechanical [Fig. 1(d)] modes; and finally (iv) a mirror region composed of eight mirror cells, placed at the end of the structure to avoid optical and mechanical leakage. The devices are fabricated at a given angle ($\theta$) defined as the counter-clockwise angle between the [100] crystalline direction and the $x$-axis of the geometry; the $z$-axis is perpendicular to the wafer plane, which in our case is aligned to the [001] direction. For a more detailed description of the fabricated design and of the fabrication process, we refer the reader to Sec. S1 of the supplementary material.

Figure 1(e) shows the basic experimental setup used to measure both the optical and mechanical properties of the devices. It consists of a tunable laser connected to an optical fiber circuit leading to a tapered fiber that couples light to the integrated tapered waveguides in our devices. Using a circulator before the tapered fiber, we recover the reflection signal from our devices. With the aid of a data acquisition card and a slow photodetector, we measure the optical response of the cavities while slowly scanning the laser frequency, allowing us to characterize their optical response as a function of the detuning $\Delta$ between the laser and the optical mode frequency, as shown in Fig. 1(f). A fast detector attached to an electrical signal analyzer (ESA) is used to measure the Power Spectral Density (PSD) of the optical signal, showing the transduction of the mechanical spectrum due to Brownian motion. The optomechanical coupling is then measured by comparing the intensity of the mechanical peaks with the intensity of a calibrated side-band introduced by a phase modulator, as proposed in Ref. 21.

In order to understand the fundamental impact of the mechanical anisotropy on the optomechanical coupling rate and mechanical mode confinement, we use Finite Element Method (FEM) simulations. Initially, we explore how $\theta$ affects the band structure of a mechanical waveguide based on the 1D mirror unit cell of our devices [Fig. 2(a)]. These propagating modes are classified according to the symmetries of the waveguide, which are a composition of the symmetries arising from the unit-cell geometry and the silicon material properties. Understanding in detail such symmetries will allow us to better appreciate the behavior of the whole device, encompassing the mirror and the defect region.

The unit cell geometry in Fig. 2(a) presents symmetry with respect to inversion about the $y$- and $x$-axes ($\sigma_y$ and $\sigma_x$); nevertheless, Floquet periodicity over the $x$-axis is such that $\sigma_x$ symmetry is only valid for modes at the center or at the edges of the Brillouin zone ($k_x = 0$ or $k_x = \pi/a$). The components of the silicon stiffness tensor can also be classified according to the $\sigma_x$ and $\sigma_y$ symmetries. The basic components $C_{11}$, $C_{12}$, and $C_{66}$ present even symmetry, while the component $C_{16}$, which couples compressive and shear stresses, is the only one that presents odd symmetry [Fig. 2(c)].

Due to the $C_{16}$ component, in general, the symmetry that is shared between the unit cell geometry and the material properties is a rotation of $\pi$ over the $z$-axis ($R_z^\pi$). Nevertheless, for $\theta = 0$ and $\theta = \pi/4$, the $x$-axis is aligned with the [100] and [110] crystallographic directions of silicon, respectively, restoring the $\sigma_y$ and $\sigma_x$ symmetries as the $C_{16}$ component is null at these angles [Fig. 2(c)].

In Fig. 2(d), we present the mechanical band diagram for $\theta = 0$, where the colored dots represent modes with even symmetry regarding $\sigma_y$ ($\sigma_y = +1$). The RGB color of the dots indicates the ratio of the displacement energy in each one of the highlighted regions in Fig. 2(a): the C-shape (red), the interface (green), and the snowflake (blue) regions. Transparent dots are modes with odd $\sigma_y$ symmetry ($\sigma_y = -1$), which do not couple with the even mechanical modes. When we consider only bands strongly confined at the C-shape region (red dots), we identify the $\sigma_y = +1$ apparent bandgap highlighted by the yellow-shaded region in Fig. 2(d). However, this is not a true bandgap since a

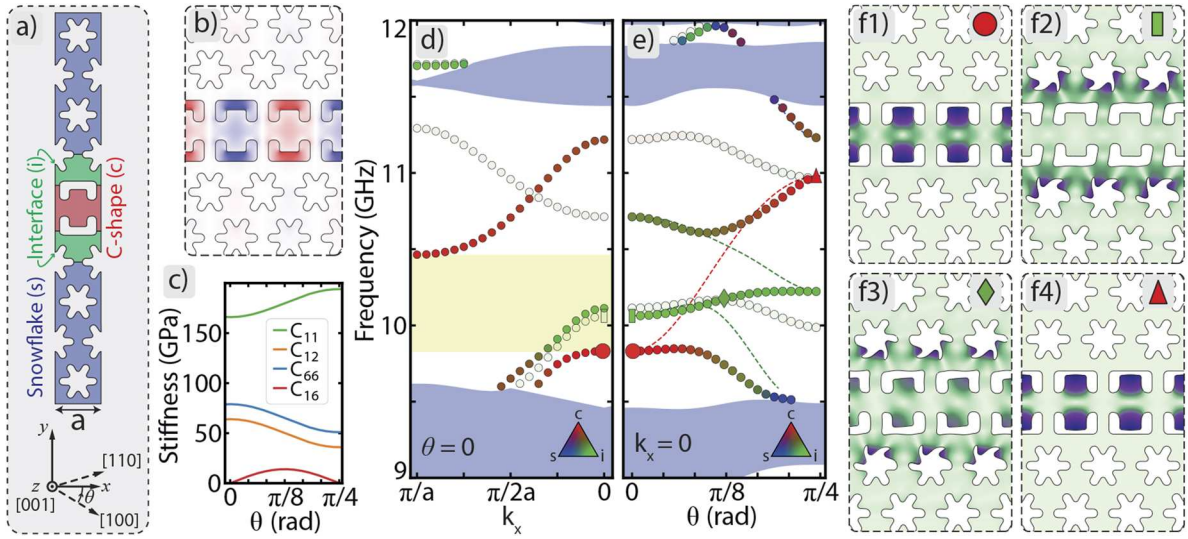


**FIG. 2.** (a) Hybrid geometry unit cell separated in different regions. (b) Electric field in the $y$ direction of the optical mode of interest. (c) Different components of the silicon stiffness tensor. (d) Mechanical band structure for $\theta = 0$. The colored circles indicate modes with $\sigma_y = +1$, while the transparent circles indicate modes with $\sigma_y = -1$. The RGB colors of the markers indicate the ratio of the displacement energy in each one of the regions of the unit cell, as indicated by the triangular legend. Notice that the $k_x$ axis is purposely inverted to approach modes at $k_x = 0$ and $\theta = 0$ in (d) and (e). (e) Mechanical band structure for $k_x = 0$ as a function of $\theta$. The colored circles indicate modes with $R_z^\pi = +1$, and the transparent circles indicate modes with $R_z^\pi = -1$. The dashed lines indicate the $R_z^\pi = +1$ modes when we force $C_{16} = 0$. The bigger markers in (d) and (e) indicate the modes presented at (f1)–(f4). (f1) The $(\sigma_x = +1, \sigma_y = +1)$ C-shape breathing mode for $k_x = 0$ and $\theta = 0$. (f2) The $(\sigma_x = -1, \sigma_y = -1)$ interface mode for $k_x = 0$ and $\theta = 0$. (f3) A $R_z^\pi = +1$ hybrid C-shape/interface mode for $k_x = 0$ and $\theta = \pi/8$. (f4) The $(\sigma_x = +1, \sigma_y = +1)$ C-shape breathing mode for $k_x = 0$ and $\theta = \pi/4$.

spurious $\sigma_y = +1$ interface band crosses it away from the $k_x = 0$ region.

The defect of our optomechanical crystal cavity was designed (see the supplementary material S2) to confine the mode from the bottom C-shape band at $k_x = 0$, which is shown in Fig. 2(f1). Despite the absence of a true phononic bandgap, one can still achieve strong confinement as long as there is no significant energy exchange between the confined mode in question and the spurious interface modes.[22] One of the factors limiting the coupling between those modes in the optomechanical cavity is the fact that at $k_x = 0$ and $\theta = 0$, the C-shape mode [Fig. 2(f1)] is the only one that presents even symmetry for both $\sigma_x$ and $\sigma_y$. Additionally, the energy transfer from the C-shape to the spurious interface modes is inhibited by the much lower quality factor of the latter.

In Fig. 2(e), we present the mechanical modes at the center of the Brillouin zone ($k_x = 0$), and the dashed lines show the band structure with $C_{16}$ set to zero. In this artificial case, the C-shape mechanical mode (red dashed line) keeps its $\sigma_y$ symmetry and remains a pure C-shape mode. Its frequency monotonically increases with $\theta$, following the $C_{11}$ component related to pure compression, while it crosses modes with distinct symmetries located at the interface (green dashed lines). However, in the real case, the shear stress promoted by the $C_{16}$ component deforms the mechanical modes, which are no longer symmetric under $\sigma_y$ and $\sigma_x$, but are still symmetric under $R_z$. The colored dots represent modes with even symmetry concerning $R_z^\pi$ ($R_z^\pi = +1$), while transparent dots present modes with $R_z^\pi = -1$. The color scheme is the same one used in Fig. 2(d) and represents the energy distribution in the geometry. As we go from $\theta = 0$ to $\theta = \pi/8$, the C-shape [Fig. 2(f1)] and interface modes with the same $R_z$ symmetry, e.g., Fig. 2(f2), couple to each other, leading to the large anti-crossing seen in Fig. 2(e). Consequently, there is no pure C-shape mode at $\theta = \pi/8$ but only mixed modes such as the one shown in Fig. 2(f3). Furthermore, the anisotropy-induced symmetry break and the strong delocalization away from the C-shape region decrease the overlap of such modes with the optical mode [Fig. 2(b)], decreasing their optomechanical coupling.

As $\theta$ goes from $\pi/8$ to $\pi/4$, the value of the $C_{16}$ component decreases toward zero, and the C-shape and interface modes become decoupled once again. At $\theta = \pi/4$, the original bandgap does not exist anymore, and a new bandgap is formed between the C-shape mode and the higher frequency snowflake modes (upper blue shaded region). There is also an interface mode very close in frequency to the C-shape mode, and although, at $k_x = 0$, these two modes have distinct $\sigma_x$ symmetry, both have similar quality factors and share $\sigma_y$ symmetry and, as such, fabrication imperfections are likely to couple them with each other. In addition, both bands present a flat dispersion near $k_x = 0$ (see supplementary material S2), making them even more susceptible to such imperfections.[19]

In the final geometry of our devices, we scaled down the lattice parameter of the snowflake crystal by 2.5% compared to the C-shape crystal, which displaces the frequency of the snowflake bands upward, allowing a larger gap between the C-shape defect mode and the snowflake modes for $\theta = \pi/4$ (see the section supplementary material S2 for a more detailed discussion). Never-

theless, as discussed in the next paragraphs, issues related to the proximity of interface modes persist in the final devices. Future optimizations of the device design should focus specifically on the interface region between the C-shape and the snowflake regions in order to move the frequency of the interface modes away from the C-shape mode.

Understanding the band structure upon which our optomechanical crystal cavity is based, we then measured the devices shown in Fig. 1(b). The mechanical spectra of devices fabricated at $\theta = \pi/4$, $\pi/8$, and 0 are shown in Figs. 3(a1)–3(a3), respectively. Figures 3(b) and 3(c) present the results of the simulation for the whole device, encompassing both the mirror and the defect region. Figure 3(b) shows the frequencies of the simulated mechanical modes as a function of $\theta$, while Fig. 3(c) shows the optomechanical coupling. The modes with the highest $g_0$ values in different frequency ranges are highlighted using the same color code as in Figs. 3(a1)–3(a3), defining mode branches. Both the experimental data and the simulations for the whole device follow the same behavior as in the waveguide simulations, where the frequency of the high $g_0$ C-shape modes increases as $\theta$ varies from 0 to $\pi/4$, with a sudden frequency jump around $\theta = \pi/8$ due to the anti-crossing of C-shape and interface modes. As shown in Fig. 3(c), when passing through such an anti-crossing, the optomechanical coupling is transferred from one branch to the other. Inside the red branch, we also find a similar behavior with $g_0$ falling steeply due to a small anti-crossing with another interface mode in between $\theta = 0$ and $\theta = \pi/12$.

The displacement profiles shown in the insets of Figs. 3(a1)–3(a3) illustrate this picture. The C-shape mode at $\theta = 0$ is concentrated in the C-shape region, overlapping with the optical mode on the airgap. At $\theta = \pi/8$, hybridization occurs due to the anisotropy, and the mechanical displacement profile extends from the C-shape into the interface region, lowering the optomechanical overlap. Finally, for $\theta = \pi/4$, the displacement profile becomes again concentrated in the C-shape region. It is interesting to notice that the optomechanical coupling is higher for $\theta = 0$ than for $\theta = \pi/4$. This happens because the mode at $\theta = 0$ is more spread along the C-shape region than the mode at $\theta = \pi/4$,[23] in such a way that the former has a better overlap with the optical mode.

The squares in Fig. 3(b) indicate the frequencies of the mechanical modes with the highest measured $g_0$.[21] The supplementary material S4 provides details on $g_0$ measurements. All devices between $\theta = 0$ and $\theta = \pi/2$ agree within 2% with the mechanical frequency simulations. However, the optomechanical couplings are not as well predicted by the simulations, as shown in Fig. 3(c), since they rely on surface and volume integrals between the mechanical and optical modes that are much more sensitive to small fabrication imperfections.

We can gain further insight by comparing multiple devices fabricated at the same crystal orientation, as shown in Figs. 3(d1) and 3(d2). For $\theta = 0$, $\pi/2$, $\pi$, and $3\pi/2$ (devices aligned with the $\langle 100 \rangle$ crystallographic direction family), the spectra are quite similar to each other, typically presenting a mechanical mode with a large optomechanical coupling that varies from 650 to 850 kHz and a secondary mode red-shifted by 50 MHz, possibly related to the second-order C-shape mode (for further discussion, see the supplementary material S3). For devices aligned with the $\langle 110 \rangle$ crystallographic direction family ($\theta = \pi/4$, $3\pi/4$, $5\pi/4$, and $7\pi/4$), the spectra of different devices are quite different from each other, with multiple broad overlapping modes. This lack of repeatability in these devices can be attributed to the flat C-shape and interface bands close to each other in the waveguide band structure, as shown in Figs. 2(e) and 3(b). Small imperfections can easily couple C-shape and interface modes, leading to these spectral differences. Our measurements



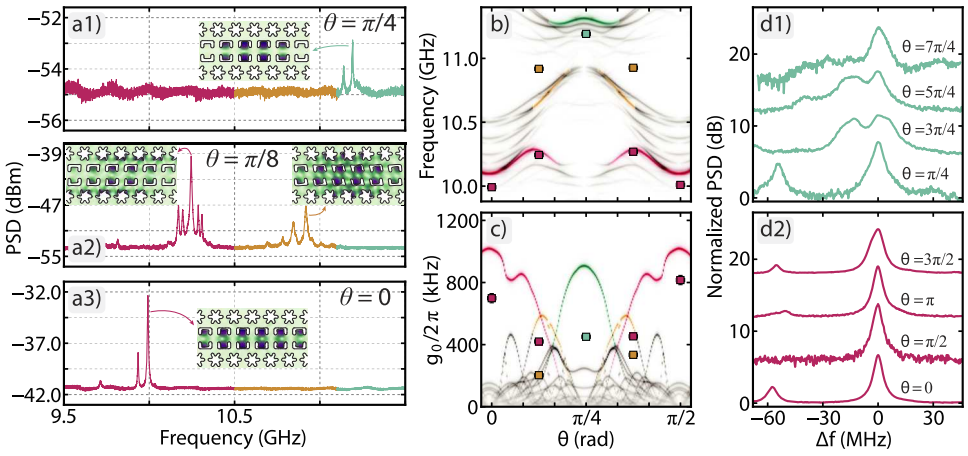


**FIG. 3.** (a1)–(a3) Power spectral density for devices of the families $\theta = \pi/4$, $\theta = \pi/8$, and $\theta = 0$ measured at room temperature and under atmospheric pressure. The insets present the displacement profiles of the indicated high $g_0$ mechanical modes. (b) Density plot showing the simulated mechanical spectra as a function of $\theta$; for clarity, only $R_z^{\pi} = +1$ modes are shown. The highlighted modes are the ones with the highest simulated $g_0$ in each of the frequency ranges. The square markers are experimental data, indicating the frequency of the higher $g_0$ modes in different devices. (c) The solid lines indicate $g_0/2\pi$ for the modes highlighted in (b); the squares are the equivalent experimental data. (d1) and (d2) Mechanical spectra of four different devices of the $\theta = \pi/4$ and $\theta = 0$ families, respectively. The spectra shown are normalized by the intensity of the PM. To enhance visibility, a common constant background is added to all spectra of the same type. The horizontal axis indicates the relative frequency shift with respect to the frequency of the highest $g_0$ mode for each spectrum, while the different spectra are shifted on the vertical axis for better visualization.

indicate that, although both orientations are subject to variations due to fabrication imperfections, devices from the $\theta = 0$ family are more robust to such imperfections than those from the $\theta = \pi/4$ family.

For the $\theta = \pi/8$ family, the comparison between simulation and experiment is more difficult as the estimated imprecision on the simulation of hybrid modes is larger (+4%) than for pure C-shape modes. Due to computational limitations, we cannot pinpoint the exact contribution of each interface mode to the measured modes; nevertheless, it is clear that multiple interface modes hybridize with the C-shape mode to form the two clusters of modes shown in Fig. 3(a2).

As a demonstration of the compatibility of such devices with quantum optomechanics experiments, we measure below 1 phonon occupancies by placing them in a dilution fridge at mK base temperatures. The phonon occupancy ($\langle n_{\mathrm{pn}} \rangle$) is measured using sideband asymmetry photon counting.[24] When a laser is fed into an optomechanical device, the interaction can be understood in terms of Stokes (anti-Stokes) processes in which one phonon is created (annihilated) while the frequency of one photon is decreased (increased) by one mechanical frequency ($\Omega/2\pi$). The likelihood of such scattering processes depends on the detuning, $\Delta$, of the laser relative to the optical resonance frequency. Stokes processes are maximum when the laser is blue-detuned by one mechanical frequency ($\Delta = +\Omega$); in contrast, anti-Stokes processes are maximum when the laser is red-detuned ($\Delta = -\Omega$).

To perform such an experiment, we used laser pulses that could be tuned to the blue and red sidebands. To avoid extra heating of the mechanical mode and guarantee that the initial state of the cavity is always the same, the laser pulses were tuned to be 100 ns wide with a 100 $\mu$s period. The scattered photons were filtered using 40 MHz wide Fabry–Pérot filters and sent to single photon detectors. The filtering efficiency of the incident laser in both sidebands was on the order of 120 dB.

Figure 4(a) shows an example of the scattering count rates obtained for the blue and red sidebands. As expected, we obtain different scattering rates for the two sidebands. In Fig. 4(b), we show the resulting occupancy for different scattering probabilities (experimentally controlled via the pulse power), showing that $\langle n_{\mathrm{pn}} \rangle$ falls as the probability is decreased. Moreover, with scattering probabilities of ~0.08% (corresponding to ~1 nW), we obtain an average occupation level lower than 0.25 phonon.

Understanding the interplay between device geometry and material anisotropy will become increasingly important as research on optomechanical devices progresses toward more complex materials, such as lithium niobate[16] or gallium phosphide,[25,26] which require specific orientation of the substrate for maximum piezoelectric coupling, and more involved bi-dimensional geometries already demonstrated to reach high quantum cooperativities.[12] Here, we have studied how the silicon mechanical anisotropy affects the properties of a bi-dimensional optomechanical crystal, showing that it can couple C-shape and interface modes, thus decreasing the overall optomechanical coupling. This effect is mitigated in devices at $\theta = 0$ and $\theta = \pi/4$, in which the device geometry shares the same symmetries as the material. We expect this interplay between the symmetries in the geometry and the material to affect any kind of optomechanical crystal fabricated in anisotropic materials. In particular, for our geometry, we identified that devices at $\theta = 0$ are more resilient to orientation fabrication imperfections. The detrimental role played by interface modes points to the large potential of interface engineering in the further optimization of our design. The latter considerations, related to interface modes, should be important in any kind of bi-dimensional optomechanical crystal composed of shield, interface, and defect regions in the same way as the geometry discussed here.

Moreover, our observation of phonon occupation below 0.25 highlights the geometry suitability of experiments operating in the quantum regime. For example, together with recent advances in coupling superconducting qubits to mechanical oscillators,[27,28] this geometry can be used as an intermediate in a microwave-optical quantum transducer,[29] where important results have already been demonstrated in a thermal noise environment of 0.64 phonons.[30] The integration of bi-dimensional geometries in such experiments could allow the use of higher scattering probabilities while maintaining a similar added noise level, reducing the optomechanical swap time, and ultimately leading to higher fidelity in the transduction process.

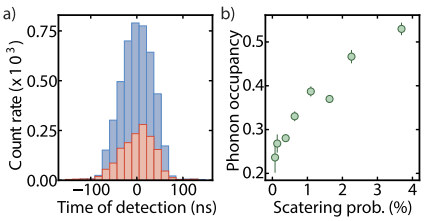


**FIG. 4.** (a) Typical asymmetry in the scattering count rates for the blue and red sidebands. (b) Measured phonon occupancy as a function of pulse scattering probability.

## SUPPLEMENTARY MATERIAL

In the supplementary material **S1**, we provide further details on C-shape geometry design and fabrication. In **S2**, we present a comprehensive description of the waveguide band structure for different crystalline orientations as well as a discussion on the mismatch between the snowflake and the C-shape unit cells. In **S3**, we discuss the identification of the smaller mode in the $\theta = 0$ spectra. Finally, in **S4**, we present a detailed discussion of the optomechanical measurements.

The authors would like to acknowledge assistance from the Kavli Nanolab Delft and CCSNano-UNICAMP with the micro-fabrication infrastructure. This work was supported by the São Paulo Research Foundation (FAPESP) through Grant Nos. 2019/01402-1, 2020/06348-2, 2020/00119-1, 2020/00100-9, 2022/07719-0, 2018/15580-6, 2018/15577-5, and 2018/25339-4, Coordenação de Aperfeiçoamento de Pessoal de Nível Superior - Brasil (CAPES) (Finance Code 001), Financiadora de Estudos e Projetos (Finep), the European Research Council (ERC CoG Q-ECHOS under Grant No. 101001005), and by the Netherlands Organization for Scientific Research (NWO/OCW) as part of the Frontiers of Nanoscience program, as well as through Vrij Programma (Grant No. 680-92-18-04).

## AUTHOR DECLARATIONS

### Conflict of Interest

The authors have no conflicts to disclose.

### Author Contributions

Cauê M. Kersul and Rodrigo Benevides contributed equally to this work.

**Cauê M. Kersul**: Conceptualization (lead); Data curation (lead); Formal analysis (lead); Investigation (equal); Methodology (equal); Software (equal); Visualization (equal); Writing – original draft (lead); Writing – review & editing (lead). **Rodrigo Benevides**: Conceptualization (lead); Data curation (lead); Formal analysis (lead); Investigation (equal); Methodology (equal); Software (equal); Visualization (equal); Writing – original draft (lead); Writing – review & editing (lead). **Flávio Moraes**: Data curation (equal); Formal analysis (equal); Investigation (equal); Methodology (equal); Software (supporting); Supervision (supporting); Writing – original draft (lead); Writing – review & editing (lead). **Gabriel H. M. de Aguiar**: Data curation (supporting); Formal analysis (supporting); Investigation (supporting); Software (equal); Writing – original draft (equal); Writing – review & editing (equal). **Andreas Wallucks**: Conceptualization (equal); Data curation (supporting); Formal analysis (supporting); Investigation (equal); Methodology (equal); Validation (equal); Writing – original draft (equal); Writing – review & editing (equal). **Simon Gröblacher**: Conceptualization (lead); Funding acquisition (lead); Project administration (lead); Supervision (lead); Writing – original draft (equal); Writing – review & editing (equal). **Gustavo S. Wiederhecker**: Conceptualization (equal); Data curation (supporting); Formal analysis (supporting); Funding acquisition (equal); Project administration (equal); Supervision (equal); Writing – original draft (equal); Writing – review & editing (equal). **Thiago P. Mayer Alegre**: Conceptualization (lead); Data curation (equal); Formal analysis (equal); Funding acquisition (lead); Investigation (equal); Methodology (equal); Project administration (lead); Software (equal); Supervision (lead); Visualization (equal); Writing – original draft (lead); Writing – review & editing (lead).

## DATA AVAILABILITY

The FEM and script files for generating each figure are available at Ref. 31. Additional data that support the findings of this study are available from the corresponding author upon reasonable request.

## REFERENCES


[1] R. Leijssen, G. R. La Gala, L. Freisem, J. T. Muhonen, and E. Verhagen, Nat. Commun. **8**, 16024 (2017); arXiv:1612.08072.

[2] K. C. Balram, M. Davanço, J. Y. Lim, J. D. Song, and K. Srinivasan, Optica **1**, 414 (2014).

[3] J. Chan, A. H. Safavi-Naeini, J. T. Hill, S. Meenehan, and O. Painter, Appl. Phys. Lett. **101**, 081115 (2012).

[4] T. P. M. Alegre, A. Safavi-Naeini, M. Winger, and O. Painter, Opt. Express **19**, 5658 (2011).

[5] G. S. MacCabe, H. Ren, J. Luo, J. D. Cohen, H. Zhou, A. Sipahigil, M. Mirhosseini, and O. Painter, Science **370**, 840 (2020).

[6] . K. Fang, M. H. Matheny, X. Luan, and O. Painter, Nat. Photonics **10**, 489 (2016).

[7] D. Navarro-Urrios, N. E. Capuj, J. Gomis-Bresco, F. Alzina, A. Pitanti, A. Griol, A. Martínez, and C. M. Sotomayor Torres, Sci. Rep. **5**, 15733 (2015).

[8] J. Chan, T. P. M. Alegre, A. H. Safavi-Naeini, J. T. Hill, A. Krause, S. Gröblacher, M. Aspelmeyer, and O. Painter, Nature **478**, 89 (2011).

[9] A. Wallucks, I. Marinković, B. Hensen, R. Stockill, and S. Gröblacher, Nat. Phys. **16**, 772 (2020); arXiv:1910.07409.

[10] N. Fiaschi, B. Hensen, A. Wallucks, R. Benevides, J. Li, T. P. M. Alegre, and S. Gröblacher, Nat. Photonics **15**, 817 (2021).

[11] R. Benevides, F. G. S. Santos, G. O. Luiz, G. S. Wiederhecker, and T. P. M. Alegre, Sci. Rep. **7**, 2491 (2017); arXiv:1701.03410.

[12] H. Ren, M. H. Matheny, G. S. MacCabe, J. Luo, H. Pfeifer, M. Mirhosseini, and O. Painter, Nat. Commun. **11**, 3373 (2020); arXiv:1910.02873.

[13] H. Sekoguchi, Y. Takahashi, T. Asano, and S. Noda, Opt. Express **22**, 916 (2014).

[14] H. Ren, T. Shah, H. Pfeifer, C. Brendel, V. Peano, F. Marquardt, and O. Painter, Nat. Commun. **13**, 3476 (2022).

[15] O. Florez, G. Arregui, M. Albrechtsen, R. C. Ng, J. Gomis-Bresco, S. Stobbe, C. M. Sotomayor-Torres, and P. D. García, Nat. Nanotechnol. **17**, 947 (2022).

[16] W. Jiang, R. N. Patel, F. M. Mayor, T. P. McKenna, P. Arrangoiz-Arriola, C. J. Sarabalis, J. D. Witmer, R. Van Laer, and A. H. Safavi-Naeini, Optica **6**, 845 (2019).

[17] R. Burgwal and E. Verhagen, Nat. Commun. **14**, 1526 (2023).

[18] A. H. Safavi-Naeini and O. Painter, Opt. Express **18**, 14926 (2010).

[19] A. H. Safavi-Naeini, J. T. Hill, S. Meenehan, J. Chan, S. Gröblacher, and O. Painter, Phys. Rev. Lett. **112**, 153603 (2014).

[20] S. Gröblacher, J. T. Hill, A. H. Safavi-Naeini, J. Chan, and O. Painter, Appl. Phys. Lett. **103**, 181104 (2013).

[21] M. L. Gorodetksy, A. Schliesser, G. Anetsberger, S. Deleglise, and T. J. Kippenberg, Opt. Express **18**, 23236 (2010).

[22] M. Eichenfield, J. Chan, A. H. Safavi-Naeini, K. J. Vahala, and O. Painter, Opt. Express **17**, 20078 (2009).

[23] This is related to the flat dispersion of the C-shape mode at $\theta = \pi/4$ which leads to a high spectral density and consequently to modes very concentrated at few defect unit-cells.

[24] S. M. Meenehan, J. D. Cohen, G. S. MacCabe, F. Marsili, M. D. Shaw, and O. Painter, Phys. Rev. X **5**, 041002 (2015).

[25] R. Stockill, M. Forsch, F. Hijazi, G. Beaudoin, K. Pantzas, I. Sagnes, R. Braive, and S. Gröblacher, Nat. Commun. **13**, 6583 (2022).

[26] K. Schneider, Y. Baumgartner, S. Hönl, P. Welter, H. Hahn, D. J. Wilson, L. Czornomaz, and P. Seidler, Optica **6**, 577 (2019).

[27] É. Dumur, K. J. Satzinger, G. A. Peairs, M.-H. Chou, A. Bienfait, H.-S. Chang, C. R. Conner, J. Grebel, R. G. Povey, Y. P. Zhong, and A. N. Cleland, npj Quantum Inf. **7**, 173 (2021).

[28] Y. Chu, P. Kharel, T. Yoon, L. Frunzio, P. T. Rakich, and R. J. Schoelkopf, Nature **563**, 666 (2018).

[29] Y. Chu and S. Gröblacher, Appl. Phys. Lett. **117**, 150503 (2020).

[30] M. Mirhosseini, A. Sipahigil, M. Kalaee, and O. Painter, Nature **588**, 599 (2020).

[31] C. M. Kersul, R. Benevides, F. Moraes, G. H. M. de Aguiar, A. Wallucks, S. Gröblacher, G. S. Wiederhecker, and T. P. M. Alegre (2022). "Data and simulation files for: "Silicon anisotropy in a bi-dimensional optomechanical cavity"," Zenodo. https://doi.org/10.5281/zenodo.7249806